11-2019

# Biochar as a filler in mixed matrix materials: Synthesis, characterization, and applications

Jeremy Lewis

Mark Miller

Jake Crumb

Maram A. Q. Al-Sayaghi

Chris Buelke

*See next page for additional authors*

# Biochar as a filler in mixed matrix materials: synthesis, characterization, and applications

Jeremy Lewis, Mark Miller, Jake Crumb, Maram Al-Sayaghi,
Chris Buelke, Austin Tesser, Ali Alshami[1]

*University of North Dakota - Department of Chemical Engineering, Grand Forks, ND*

**Abstract**

The use of mixed matrix materials (MMM) has become a major topic of research in recent years, owing to the unique properties achieved in these composites. In this work, biochar from sunflower seed hull (SSH) pyrolysis and biochar/polysulfone (PSF) MMMs were produced and characterized. The optimal pyrolysis temperature for biochar production was determined to be 500°C. The resulting biochar properties were an iodine number of 203 mg/g and pore volume of 0.595 mL/g. In MMM fabrication, the use of as little as 4% ethanol as nonsolvent in the wet phase inversion process increased the glass transition temperature by 8°C, indicating improved biochar/PSF interaction. The presence of biochar was shown to influence the surface properties of the films, creating pores in otherwise dense surfaces. The critical surface energy was also increased by the addition of biochar from 28.6 mN/m in pristine PSF to 35.7 mN/m in biochar/PSF MMMs. We identified and discussed several potential applications based on the determined properties. We have shown that biochar is a viable filler in MMM and ethanol solutions used as a nonsolvent can enhance the interfacial interaction.

**Key words**: biochar, polysulfone, nanocomposite, mixed matrix material, polymer matrix composite

[1] Corresponding author: Ali Alshami, ali.alshami@und.edu

## 1. Introduction

Mixed matrix materials (MMMs) are composites, often formed into thin films, consisting of a continuous phase (matrix) and a dispersed particle phase (filler). Over the past three decades, these materials have been investigated for various applications including membranes for separations [1-3], reinforced materials for structures [4,5], and as wound dressings [6] among others. By creating MMMs, properties of both the matrix and filler are exploited, and oftentimes enhanced, resulting in superior properties than either the matrix or filler alone. Despite the diversity of available filler materials and abundance of studies into their properties, one particular filler remains mildly researched; namely, biochar from biomass pyrolysis. Biochar exhibits distinctive properties and possess key features rendering it worthwhile to study in MMMs.

The most important aspect of MMM development is material's constituent's selection. As a result, much research has been focused on fabrication and implementation of various matrix/filler combinations. The most common class of matrix materials are polymers, due to the number of polymers available, and the simple processability of polymers into MMMs. MMMs with glassy polymers [7], rubbery polymers [8], polymer blends [9], and copolymers [10,11] have all been investigated. Both inorganic and organic type fillers have been investigated. These include clay particles [12], metal organic frameworks [2], activated carbon [13], graphene [4,8], and metal oxides [14] to name a few.

Although any polymer and filler can be combined into MMMs, their compatibility is critical and deterministic for the overall composite properties and function. Poor compatibility can result in poor matrix/filler interactions, causing void formation, reduced thermal and mechanical performance [15], and undesired permeation properties [16]. Researchers have

investigated several methods to prevent or correct poor polymer/filler compatibility [17], including functionalization of the matrix or filler [18], interfacial polymerization of monomers containing fillers [19], matching the polarity of the matrix/filler [20], and using nano sized fillers [21].

Biochar as a filler material in MMMs functional composites has been minimally investigated as an effective element in MMMs. Biochar particles, a solid product of biomass pyrolysis, are porous, with high specific surface areas, and can be easily processed into sizes ranging from nanometers to millimeters. Due to the nature of biomass and biomass degradation, biochars tend to possess surface functional groups that are dependent on the biomass precursor and pyrolysis conditions [22]. Biochar particles' functionality and porosity offer ample binding sites for the polymer matrix; thus, increasing the possibility of strong interfacial interactions [23]. Hence, owing to these key and significant features, in addition to the cost-effect production methods, biochars present an invaluable material to probe as a filler of MMM constructs.

Another critical aspect of MMM development and performance is the method of fabrication and processing selection. One of the most common fabrication techniques for creating MMM films involve phase inversion of a dissolved polymer/filler solution [24]. The wet phase inversion technique is performed by casting a dissolved polymer solution, then introducing it to a nonsolvent. Liquid-liquid demixing occurs instantly, resulting in precipitation of a thin polymeric film. [25]. The two key parameters of wet phase inversion are the quaternary components of polymer/filler/solvent/nonsolvent system and temperature. The dry phase inversion method utilizes solvent evaporation for film precipitation [26]. In this case, a cast solution is heated for enough time to allow all the solvent to evaporate. The rate of evaporation, and thus the environmental conditions, play an important role. Combinations of these two

techniques have also been thoroughly investigated, known as dry/wet phase inversion. Each method results in films with unique surface and cross sectional morphologies. Other fabrication methods have been used for MMM development, but usually involve a phase inversion step as one step in the process. For example, spin coating utilizes a spinning wheel to spread a film, rather than a casting blade, then phase inversion is used to precipitate the film [27].

Despite a thorough understanding of phase inversion processes, there has been minimal emphasis on how polymer/filler interaction is influenced by fabrication technique. The phase inversion process can be highly influential in the polymer/filler interaction due to the complex demixing that occurs upon precipitation. Biochar is highly adsorptive, so it is anticipated that when used as a filler, it has complex interactions between each of solvent, nonsolvent, and polymer due to the adsorption capacity of the biochar to each of these components.

In this work, we report on a study of filler-matrix interaction and influence of fabrication method on MMM films. In particular, we present characterization of MMM films consisting of a biochar filler embedded in a polysulfone (PSF) matrix. The biochar is synthesized from sunflower seed hulls (SSH), and the film is produced by the wet phase inversion method in ethanol solutions. We use this combination to investigate the viability of biochar as a filler in MMMs and to investigate the role of nonsolvent on the biochar/PSF interaction.

## 2. Materials and Methods

### 2.1. Materials

SSH were supplied by CHS Sunflower, Grandin, ND, USA. Polysulfone (35,000 Da PSF) and anhydrous dimethyl formamide (99.8% DMF) were purchased from Sigma Aldrich Co., USA. Compressed analytical-grade gases including argon (Ar 99.998%), nitrogen ($N_2$ 99.998%)

and air were purchased from Praxair Co., USA. PSF was dried in an oven at 105°C before use in an ambient atmosphere. DMF was used without further purification. Chemicals used for iodine number determination (sodium thiosulfate (99%), iodine (>99.8%), potassium iodide (>99%, and potassium iodate (>98%)) were purchased from Sigma Aldrich Co., USA. Fuming hydrochloric acid was purchased from Fisher Scientific Co., USA. Butanol (99%) was used for pore volume estimation and was purchased from Fisher Scientific Co., USA. Polyethylene glycol (200 Da PEG) was used for surface energy calculations and was purchased from Sigma Aldrich Co., USA.

### 2.2. Biochar Synthesis via Slow Pyrolysis Reaction

Between 50 and 70g of SSH were loaded into a Thermolyne 21100 tube furnace reactor with a heating rate controller and temperature indicator shown in Figure 1. A stainless steel tube reactor with flanges on both ends was used as the reaction vessel. Argon (Ar) was used as the inert gas to displace oxygen at a rate of 2 mL/min. The reactor was purged with Ar for at least five minutes before heating. The reactor was set to heat at a rate of 15°C/min to various temperatures then allowed to slowly cool to room temperature under continuous Ar flow. Produced oils and tar were condensed in a water bath upon exiting the reactor, and volatiles were allowed to vent. Once cooled, the biochar was collected from the furnace and washed several times with distilled water, then dried in an oven at 105°C for several hours.

Once dried, the weight of biochar was recorded and the yield was calculated according to Equation 1:

$$\text{Yield } \% = \frac{\text{Biochar Weight}}{\text{Initial Sample Weight}} * 100\% \quad (1)$$

The biochar was then ground to a fine powder and sieved with an ASTM #270 mesh (53 microns) for one hour using a vibrating shaker.

### 2.3. MMM Film Fabrication

PSF was dissolved in DMF for an overall composition of 20% by mass of polymer. It is worth noting, DMF was chosen based on the solubility of biochar in DMF shown in supplemental material S1. While the solubility in the polymer phase is highly important, the solubility in the solvent was considered here for optimal results. The solution was stirred for at least 12 hours, or until completely dissolved, at room temperature with a mixing speed of 60 rpm. Biochar was then added at 1% by mass relative to the polymer phase, then mixed for at least 6 hours at a rate of 60 rpm. The solution was cast using a casting knife, then precipitated at room temperature in a nonsolvent of distilled water or ethanol solutions. The films were rinsed thoroughly with distilled water and dried at room temperature before analysis.

### 2.4. Biochar Characterization

#### 2.4.1. Ultimate and Proximate Analysis

Ultimate analysis (CHN) was performed on raw SSH and biochar by Atlantic Microlab Inc., USA. Proximate analysis was performed using a thermogravimetric analyzer with differential scanning calorimetry (TGA/DSC) with a model SDT Q-600 analyzer. Samples were heated at a rate of 15°C/min in $N_2$ or air from room temperature to 900°C.

#### 2.4.2. Surface Area and Pore Volume

The biochar surface area was measured by means of iodine adsorption number according to ASTM standard 4607-94 [28]. In short, an iodine solution was put in contact with biochar. The residual was filtered and titrated with sodium thiosulfate to the endpoint. The iodine number

is defined as the amount of iodine adsorbed per gram of biochar at a residual concentration of 0.02 N. The total pore volume was estimated based on thermogravimetric methods developed by Pan et. al., (1996) [29] and Mercuri et. al. (2006) [30]. Biochars were mixed with butanol, and the butanol desorption rate was quantified from changes in TGA/DTG curves. The pore volume was calculated based on empirical correlations listed in the supplemental material S2.

#### 2.4.3. Scanning Electron Microscopy (SEM)

The particle size distribution was measured by analyzing SEM images with the open source software Image J [31]. Images were taken using a Hitachi SU8010 field emission scanning electron microscope. The number frequency average was taken based on the largest diameter of each particle. Biochar pores and surface morphology were also investigated by SEM analysis.

#### 2.4.4. Functional Groups

Functional groups were analyzed using a ThermoNicolet NEXUS 460 FTIR equipped with a ZnSe crystal and DTGS detector. The spectra were tested in attenuated total reflection mode.

### 2.5. MMM Film Characterization

#### 2.5.1. Differential Scanning Calorimetry (DSC)

A PerkinElmer DSC was used to measure glass transition temperature ($T_g$) of MMMs. About 5mg of samples were tested in aluminum pans. The method consisted of three cycles of heating from 0 to 200°C at a rate of 20°C $min^{-1}$, and were held isothermal at 0 and 200°C for two minutes to allow the sample to equilibrate.

#### 2.5.2. Thermogravimetric Analysis (TGA)

TGA was performed on MMMs using the equipment described in section 2.4.1. About 10mg of film were analyzed. The degradation temperature ($T_d$) was recorded based on the maximum of the differential thermogravimetric (DTG) curve.

#### 2.5.3. Scanning Electron Microscopy (SEM)

MMM morphology was investigated using a Hitachi SU8010 field emission scanning electron microscope. MMMs were fractured with liquid nitrogen to expose the cross section, then sputter coated for 30 seconds with carbon.

#### 2.5.4. Contact Angle and Surface Energy

The contact angle of MMM films was measured by a sessile drop method described by Costa et al. (2018) [32]. In short, an image was taken of a 20 μL drop from the top view. The diameter was measured, and the contact angle was calculated assuming a spherical cap geometry. Further detail on this method is described in the supplemental material S3. The critical surface energy was calculated based on the contact angle of PEG solutions according to the Zisman method [33,34], as described in more detail in section 3.2.

## 3. Results and Analysis

### 3.1. Biochar Fabrication and Analysis

In order to determine a suitable pyrolysis temperature of SSH, the pyrolysis reaction was investigated by TGA, as it has been shown before that the optimal reaction temperature can be predicted in this fashion [35]. From the DTG curve in Figure 2a, it is apparent that weight loss occurs at two temperature ranges. The first peak near 100°C is attributed to moisture loss whereas the second peak occurs near 350°C and is a result of cellulose, hemicellulose, and lignin degradation. The degradation rate levels off at 450°C. Thus at 500°C, the major degradation is

complete. To complement this, yield was taken after pyrolysis at several temperatures and is shown in Figure 2(b). As expected, the yield decreases as temperature increases until about 500°C where there is little change. It is worth noting that the theoretical yield of biochar based on the TGA curve does not always match the actual yield, primarily due to the residual uncharred biomass. Based on these two results, 500°C was chosen as the optimal pyrolysis temperature. In this case, the optimum temperature results in low yield but desirable physicochemical properties.

From the ultimate analysis results shown in Table 1, it is clear that biochar is richer in carbon and nitrogen compared to the raw SSH. Likewise, the presence of oxygen and hydrogen decreased after pyrolysis. This is to be expected; as pyrolysis occurs, oxygenated functional groups easily break apart and leave behind a graphite like structure, which is also concluded by the fixed carbon content of each species. The pore volume and iodine number demonstrate the formation of pores within the biochar, creating additional surface area for gas-solid and liquid-solid adsorption.

After sieving the biochar, the number average diameter was taken and organized into bin sizes of 2.5 microns. As shown in the histogram in Figure 3a, there was a higher percentage of smaller particles. Had aggregates been considered, the number average would have been highly skewed as a significant number of aggregates were observed as seen in Figure 3b. However, some particles larger than the mesh size (55 microns) were measured. The appearance of particles larger than the mesh size can be explained by their variation in geometry: larger particles could pass if oriented on their smaller axis.

FTIR spectra of the biochar is shown in Figure 4. The baseline shift seen after 2000 $cm^{-1}$ is apparent and is common for carbonaceous materials due to strong absorption bands in that region. This causes a refractive index response very close to that of the ZnSe crystal, resulting in a noticeable shift. Regardless of this, the peaks are readily visible. Their position and corresponding functional groups are summarized in Table 2. The spectra indicate the presence of oxygenated and nitrogenized functional groups with alkane, alkene, and alkyne linkages supported in aromatic structures.

### 3.2. MMM Fabrication and Analysis

The wet phase inversion method can be described by a solvent/nonsolvent/polymer ternary phase diagram as shown in Figure 5. The binodal line represents the region in which liquid-liquid demixing begins and phase separation occurs. Experimentally, the binodal line is determined by titration with nonsolvent to the cloud point. It is apparent that there is a difference in binodal placement if pure water or pure ethanol are used as the nonsolvent. Various concentrations of ethanol in water are expected to lie within these two curves, so they were not recorded.

MMM films loaded with 1% (relative to the polymer phase) of biochar were precipitated in various ethanol solutions containing between 0 and 20 vol.% ethanol. The $T_g$ of each was measured since it is understood that the polymer/filler interaction in MMMs can be examined by measuring $T_g$ of the composite [36,37]. The $T_g$ was taken as the inflection point from DSC thermograms as seen in Figure 6a. The extracted values shown in Figure 6b demonstrate there is a linear trend until about 4 vol.% ethanol, then flattens off. This analysis revealed some interesting features of the biochar/PSF MMM.

FTIR spectra of each film were taken to rule out the possibility of chemical reactions caused by ethanol, and to investigate possible migration of biochar to either surface of the film. Both top and bottom of the films were observed, but due to exact matches between sides, only the top is shown. The spectra shown in Figure 7 reveal that no chemical reactions took place during the phase inversion process, as all peaks are consistent between samples and match the spectra of pure PSF reported elsewhere [38]. The most important peaks and corresponding wavenumbers that identify PSF are aryl ethers (1270-1230 $cm^{-1}$), aryl sulfones (1170-1135 $cm^{-1}$), and methyl groups (2970-2950 $cm^{-1}$).

The cross section and surface morphology were investigated using SEM. No morphological differences were apparent between films made with and without ethanol in the coagulation bath as seen in Figures 8a and 8b. The surface appears dense and the cross section is asymmetric with a thin top skin and spongy support structure. While the presence of ethanol did not appear to have an effect on morphology, the influence of biochar loading significantly influenced the surface. To demonstrate this, MMMs were loaded with 10 and 40 wt.% biochar relative to the polymer phase. The 10% loaded films showed surface pore formation on the order of 1 micron, shown in Figure 9c. At 40%, the pores appear larger, on the order of 10 microns. However, pore blockage was apparent as depicted in Figure 9d.

The surface energy of MMMs is another important parameter that allows for the prediction of properties such as permeability and adsorption of fluids. One technique to measure this is the Zisman method, which is an empirical method that allows for the evaluation of the critical surface energy ($\gamma_c$). The procedure is commonly employed for quick estimations of solid surface energy. The procedure and derivation have been discussed elsewhere in detail [39,40]. In short, the known liquid surface energy of several different liquids, $\gamma_l$, is plotted verses $\cos(\theta)$, where $\theta$

is the contact angle between the solid and liquid drop. The linear line is extrapolated to the point where $\cos(\theta) = 1$. The value of surface energy at this point is $\gamma_c$.

PSF is readily dissolved in many common liquids with known $\gamma_l$. This tremendously reduces the number of liquids available for analysis because drops will quickly dissolve films and not form a drop upon contact. In this case, three different liquids were examined: distilled water, PEG-200, and a 15 vol.% PEG-200 in distilled water. The contact angle measurements and $\gamma_l$ values are displayed in Table 3. All contact angles are the average of at least three measurements. The contact angles of each liquid on the 1% loaded biochar films formed in 4 vol.% ethanol were compared to films prepared without biochar to gain a better understanding of the influence biochar has as the filler material. All values were recorded in Table 3 and were used to construct a Zisman plot (Figure 10).

## 4. Discussion

In fabricating biochar from SSH pyrolysis, yield, surface area (iodine number), pore volume, and functional groups are key parameters that are influenced by pyrolysis temperature. It was shown that the yield decreases with increasing pyrolysis temperature at a rate of between 5%-10% per 100°C. Furthermore, it is well accepted that there exists a tradeoff between the yield and some of the physical properties. This is important to realize because at moderate temperatures, a low yield typically indicates the point where surface area and pore volume are highest. This point is distinguishable in Figure 2. Thus if pyrolysis is performed at lower temperatures, the iodine number and pore volume will likely be lower, despite the higher yield. The same is true at higher temperatures. In this case, pores collapse, resulting in lower surface area and pore volume. This optimal pyrolysis phenomena is commonly encountered [22].

There are several implications to potential applications based on the biochar characteristics. Firstly, the iodine number of 203 mg/g is reasonable compared to other biomasses [43]. Depending on the desired application, this iodine number could be sufficient. For example, if used as a conducting material, the surface area may not influence conductive properties. If used for separations, higher adsorption capacity may prove beneficial, so further treatment of the biochar may be necessary. The opposite is applicable for antimicrobial film applications where much of the antimicrobial properties are a result of microbe repulsion. Higher surface area allows more space for microbes to collect, thus reducing the antimicrobial properties [44].

The particle size and size distribution are expected to have some significant effects. It was shown in Figure 3 that the average biochar particle size obtained was 18.1 ± 4.0 microns (at 95% confidence) with a median of 15.7 microns. Because the particles are relatively large, the MMM thickness is limited to the size of the largest particles. If thinner films are formed, there is a higher chance of surface ruptures. Considering small particles tend to perform better in MMMs, the presented size distribution lends itself to a mixture of interactions in the MMM. Some of which favor strong interactions, some favor weaker interactions. Since the size distribution is skewed toward smaller particles, those interactions may be dominant.

The functional groups seen in the biochar are more so important to polymer/filler interaction than the size distribution. The FTIR spectra in Figure 4 indicate the presence of oxygenated and nitrogenized functional groups with alkane, alkene, and alkyne linkages supported in aromatic structures. The positive ends of the polar oxygenated/nitrogenized functional groups can produce dipole interactions between them and the sulfone group in PSF. However, the coupling of biochar size, size distribution, pore volume, surface area, and functional groups actually showed poor interaction between the biochar and PSF when water was

used as the nonsolvent. This is indicated by a $T_g$ of 181°C ±1.5°at 95% confidence, which is lower than the 185°C $T_g$ of pure PSF. Thus, the nonsolvent choice was shown to be significant. A shift in the ternary binodal line indicated that when using ethanol as the nonsolvent, the demixing process speeds up, resulting in faster demixing. Physically, this is significant because the solvent will quickly diffuse from the polymer rich region to the nonsolvent, causing a reduction in the hydrated layer surrounding the biochar [45]. This likely results in better adhesion between the biochar and PSF. This is supported by the increase in $T_g$ with increasing amounts of ethanol in the nonsolvent described in Figure 6. The $T_g$ at 4 vol.% ethanol of about 188°C ±1° at 95% confidence, is indicative of this improved interaction. Considering this, it is anticipated that other thermo-mechanical properties are also improved. The use of 4% ethanol in the coagulation bath offers a simple method to improve the interaction between biochar and PSF. It can possibly improve the interaction between other combinations of polymer/filler and should be investigated.

Moreover, the absence of characteristic FTIR peaks of the biochar on the top and bottom surface of the MMMs indicated that there was no migration to either side of the film, and the biochar remained within the cross section. Considering the migration of fillers to the surface of MMMs have been observed before [46], the concentration of biochar at the top surface may have been too dilute to measure its characteristic peaks by FTIR.

Another important thermal property is the degradation temperature ($T_d$), defined here as the temperature where the DTG curve is maximum. The $T_d$, regardless of ethanol concentration in the coagulation bath was near 543 ±7°C at 95% confidence. However, this is lower than what is typically reported for PSF [38]. This is likely a result of thermal degradation of the biochar, $T_d$ of about 300°C, occurring before that of PSF. This has two pronoun effects on the overall $T_d$.

Firstly, the degradation of biochar leaves behind void spaces, resulting in a more unstable matrix. Secondly, the decrease in mass of the sample at lower temperatures causes a faster response in $T_d$, which is a well-known occurrence in TGA [47]. Therefore, the thermal stability of the biochar ultimately limits that of the MMM, rather than acting as a thermal stabilizer. The implications are the combination of biochar/PSF MMMs cannot be used in high temperature applications that exceed 300°C, else the biochar would thermally degrade leaving behind an unstable MMM. Many applications involving films are often performed at temperatures much lower than 300°C, so this may not restrict the use of these MMMs.

The cross sectional and top surface morphology of the MMMs shown in Figure 8 also give insight into the potential use. MMMs with dilute biochar showed dense top surfaces with spongy cross sections with a thin dense layer. This lends itself for use in separations where the dense surface of the PSF acts as the selective barrier. Being thin, this layer is expected to exhibit high flux to gases when subject to high pressures. When higher concentrations of biochar were added to the MMMs, surface pores formed. This along with adding pore forming agents could create suitable materials for liquid phase separation applications where surface pores are necessary. Furthermore, very high concentrations of biochar tend to cause surface defects such as ruptures and pore blockage. These defects are undesired and result in materials that are unusable for most applications: poor mechanical stability, poor thermal stability, inhomogeneity in the surface. Clearly there is a limit in biochar loading, much like other filler materials.

Lastly, it was apparent the critical surface energy of the biochar loaded film (35.7 mN/m, regardless of ethanol concentration in nonsolvent) was higher than that of the pure PSF (28.6 mN/m). This analysis is depicted in Figure 7. While both surfaces are considered “low energy”, this indicated the surface of the biochar loaded film has a higher affinity to adsorb liquids. In

turn, this leads to higher degrees of wetting for a larger array of liquids. Thus the biochar loaded MMMs are more versatile in regards to liquid phase separation applications where complete surface wetting is attributed to better separation performance.

Biochar/PSF MMMs can also be worthwhile to study in electronic applications where a moderate dielectric constant and thermal stability are required. Pure PSF has a dielectric constant near 3.1, depending on molecular weight. Considering biochar is electrically conductive [48], much like other carbonaceous materials, the dielectric constant of these MMMs is likely higher. The films would also have a tunable dielectric constant based on the biochar loading thus, would be ideal and versatile for the dielectric end of a monopole antenna. This, coupled with the wetting ability of many different liquids on the surface, can lead to a variety of liquid sensing capabilities. However, care must be taken as inhomogeneous loading could lead to anisotropic electrical properties [49]. Under low pressure conditions, these MMM characteristics also find useful traits in film packaging applications. Biochar tends to be antimicrobial, resulting in antimicrobial MMMs [50]. This, coupled with a dense top layer, limits penetration of unwanted moisture or bacteria when subject to a range of temperatures at normal pressures, which is an ideal case for film packaging.

## 5. Conclusion

We have shown that biochar made from SSH pyrolysis at 500°C is a feasible filler in a PSF matrix made by wet phase inversion. This work addressed and offered a solution to one of the most prioritized problems with MMMs, poor polymer/filler interaction. By using a solution of 4 vol.% ethanol in distilled water as the nonsolvent, the $T_g$ was shown to increase, indicating better biochar/PSF interaction. This reaches far beyond the biochar/PSF combination, as it can potentially improve the interaction between other filler/matrix combinations. The presence of

ethanol in the coagulation bath did not influence surface or cross sectional morphology or surface energy. However, the presence of biochar in the PSF did influence the surface morphology and surface energy compared to pristine PSF. Insight into potential applications were discussed. In future works, the further application of biochar/PSF MMMs can be investigated as they present promising characteristics.

**Acknowledgements**

This research was supported by North Dakota Department of Commerce (Fund 16-08-J1-144), NASA EPSCoR (NNX15AK49A), and ND EPSCoR (FAR0023660). The authors would like to acknowledge Yuquian Xing from UND department of Chemistry for assistance with SEM. The authors also declare no conflicts of interest.

**References**

1. P.S. Goh, A.F. Ismail, S.M. Sanip, B.C. Ng, M. Aziz. Recent advances of inorganic fillers in mixed matrix membrane for gas separation. Separation and Purification Technology 2011;81:243-264.

2. Dechnik J, Sumby CJ, Janiak C. Enhancing Mixed-Matrix Membrane Performance with Metal–Organic Framework Additives. Crystal Growth & Design 2017;17(8):4467-4488.

3. Bastani D, Esmaeili N, Asadollahi M. Polymeric mixed matrix membranes containing zeolites as a filler for gas separation applications: A review. Journal of Industrial and Engineering Chemistry 2013;19(2):375-393.

4. Hu K, Kulkarni DD, Choi I, Tsukruk VV. Graphene-polymer nanocomposites for structural and functional applications. Progress in Polymer Science 2014;39(11):1934-1972.

5. Rodríguez-González J, Rubio-González C, Jiménez-Mora M, Ramos-Galicia L, Velasco-Santos C. Influence of the Hybrid Combination of Multiwalled Carbon Nanotubes and Graphene Oxide on Interlaminar Mechanical Properties of Carbon Fiber/Epoxy Laminates. Appl Compos Mater 2018;25(5):1115-1131.

6. Kamel NA, Abd El-Messieh SL, Saleh NM. Chitosan/banana peel powder nanocomposites for wound dressing application: Preparation and characterization. Materials science & engineering. C, Materials for biological applications 2017;72:543-550.

7. Etienne S, Becker C, Ruch D, Germain A, Calberg C. Synergetic effect of poly(vinyl butyral) and calcium carbonate on thermal stability of poly(vinyl chloride) nanocomposites investigated by TG–FTIR–MS. J Therm Anal Calorim 2010;100(2):667-677.

8. Chen D, Chen S, Yi R, Xu T, Gordin ML, Wang D. Facile synthesis of graphene–silicon nanocomposites with an advanced binder for high-performance lithium-ion battery anodes. Solid State Ionics 2014;254:65-71.

9. El Miri N, Abdelouahdi K, Zahouily M, Fihri A, Barakat A, Solhy A, El Achaby M. Bio-nanocomposite films based on cellulose nanocrystals filled polyvinyl alcohol/chitosan polymer blend. Journal of Applied Polymer Science 2015;132(22):n/a.

10. Anson M, Marchese J, Garis E, Ochoa N, Pagliero C. ABS copolymer-activated carbon mixed matrix membranes for CO 2/CH 4 separation. Journal of Membrane Science 2004;243(1):19-28.

11. Marchese J, Anson M, Ochoa NA, Prádanos P, Palacio L, Hernández A. Morphology and structure of ABS membranes filled with two different activated carbons. Chemical Engineering Science 2006;61(16):5448-5454.

12. Kotal M, Bhowmick AK. Polymer nanocomposites from modified clays: Recent advances and challenges. Progress in Polymer Science 2015;51:127-187.

13. Tijink MSL, Wester M, Sun J, Saris A, Bolhuis-Versteeg LAM, Saiful S, Joles JA, Borneman Z, Wessling M, Stamatialis DF. A novel approach for blood purification: Mixed-matrix membranes combining diffusion and adsorption in one step. Acta Biomaterialia 2012;8(6):2279-2287.

14. Yan B, Wang Y, Wu X. Preparation and characterization of ZnO/ZnS core/shell nanocomposites through a simple chemical method. Advanced Composite Materials 2018;27(4):387-396.

15. Hu J, Jia X, Li C, Ma Z, Zhang G, Sheng W, Zhang X, Wei Z. Effect of interfacial interaction between graphene oxide derivatives and poly(vinyl chloride) upon the mechanical properties of their nanocomposites. J Mater Sci 2014;49(7):2943-2951.

16. Hoang Vinh-Thang, Serge Kaliaguine. Predictive Models for Mixed-Matrix Membrane Performance: A Review. Chemical Reviews 2013;113(7):4980-5028.

17. Rong MZ, Zhang MQ, Ruan WH. Surface modification of nanoscale fillers for improving properties of polymer nanocomposites: a review. Materials Science and Technology 2006;22(7):787-796.

18. Li Z, Chu J, Yang C, Hao S, Bissett MA, Kinloch IA, Young RJ. Effect of functional groups on the agglomeration of graphene in nanocomposites. Composites Science and Technology 2018;163:116-122.

19. Sorribas S, Gorgojo P, Tellez C, Coronas J, Livingston AG. High Flux Thin Film Nanocomposite Membranes Based on Metal-Organic Frameworks for Organic Solvent Nanofiltration. JOURNAL OF THE AMERICAN CHEMICAL SOCIETY 2013.

20. Paul DR, Robeson LM. Polymer nanotechnology: Nanocomposites. Polymer 2008;49(15):3187-3204.

21. Mousa M, Dong Y. Strong Poly(Vinyl Alcohol) (PVA)/Bamboo Charcoal (BC) Nanocomposite Films with Particle Size Effect. ACS Sustainable Chemistry & Engineering 2018;6(1):467-479.

22. Wu-Jun Liu, Hong Jiang, Han-Qing Yu. Development of Biochar-Based Functional Materials: Toward a Sustainable Platform Carbon Material. Chemical Reviews 2015;115(22):12251-12285.

23. Mousa M, Dong Y, Davies IJ. Eco-friendly polyvinyl alcohol (PVA)/bamboo charcoal (BC) nanocomposites with superior mechanical and thermal properties. Advanced Composite Materials 2018;27(5):499-509.

24. Buelke C, Alshami A, Casler J, Lewis J, Al-Sayaghi M, Hickner MA. Graphene oxide membranes for enhancing water purification in terrestrial and space-born applications: State of the art. Desalination 2018.

25. Guillen GR, Pan Y, Li M, Hoek EMV. Preparation and Characterization of Membranes Formed by Nonsolvent Induced Phase Separation: A Review. 2011.

26. Pinnau I, Koros WJ. Structures and gas separation properties of asymmetric polysulfone membranes made by dry, wet, and dry/wet phase inversion. Journal of Applied Polymer Science 1991;43(8):1491-1502.

27. Hu P, Yan L, Zhao C, Zhang Y, Niu J. Double-layer structured PVDF nanocomposite film designed for flexible nanogenerator exhibiting enhanced piezoelectric output and mechanical property. Composites Science and Technology 2018;168:327-335.

28. Activated carbon. Standard test method for determination of iodine number. 2015.

29. Pan D, Jaroniec M, Klinik J. Thermogravimetric evaluation of the specific surface area and total porosity of microporous carbons. Carbon 1996;34(9):1109-1113.

30. Mercuri LP, Matos JR, Li Z, Jaroniec M. Comparative thermogravimetric and adsorption study of highly ordered mesoporous materials. Journal of Colloid and Interface Science 2006;296(1):377-380.

31. Syed R, Sobh N, Ravaioli U, Popescu G, Mohamed M. imageJ. 2015.

32. Costa E, Aquilano D. Experimental Value of the Specific Surface Energy of the Cleavage {10.4} Calcite Rhombohedron in the Presence of Its Saturated Aqueous Solution. Crystals 2018;8(6):238.

33. Zisman WA. Relation of the Equilibrium Contact Angle to Liquid and Solid Constitution  Advances in Chemistry 1964:1-51.

34. Kabza KG, Gestwicki JE, McGrath JL. Contact Angle Goniometry as a Tool for Surface Tension Measurements of Solids, Using Zisman Plot Method. A Physical Chemistry Experiment. Journal of Chemical Education 2000;77(1):63.

35. Tsai W, Chang C, Lee S, Wang S. Thermogravimetric Analysis of Corn Cob Impregnated With Zinc Chloride for Preparation of Activated Carbon. Journal of Thermal Analysis and Calorimetry 2000;63(2):351-357.

36. Kumar SK, Li C, Schadler LS, Bansal A, Cho K, Yang H, Benicewicz BC. Quantitative equivalence between polymer nanocomposites and thin polymer films. Nature Materials 2005;4(9):693-698.

37. Schadler LS, Kumar SK, Benicewicz BC, Lewis SL, Harton SE. Designed Interfaces in Polymer Nanocomposites: A Fundamental Viewpoint. MRS Bulletin 2007;32(4):335-340.

38. Adewole JK, Ahmad AL, Ismail S, Leo CP, Sultan AS. Comparative studies on the effects of casting solvent on physico-chemical and gas transport properties of dense polysulfone membrane used for CO2/CH4separation. Journal of Applied Polymer Science 2015;132(27):n/a.

39. Koopal LK. Wetting of Solid Surfaces: Fundamentals and Charge effects. Advances in Colloid and Interface Science 2012;179-182:29-42.

40. Gindl M, Gindl W, Sinn G, Reiterer A, Tschegg S. A comparison of different methods to calculate the surface free energy of wood using contact angle measurements. Colloids and Surfaces A: Physicochemical and Engineering Aspects 2001;181(1):279-287.

41. DataPhysics Instruments. Surface tension values of some common test liquids for surface energy analysis.

42. Amooey AA, Fazlollahnejad M. Study of Surface Tension of Binary Mixtures of Poly (Ethylene Glycol) in Water and Poly (Propylene Glycol)
in Ethanol and its Modeling Using Neural Network  Iranian Journal of Chemical Engineering 2014;11(1):19-29.

43. POWAR RV, GANGIL S. Effect of temperature on iodine value and total carbon contain in bio-char produced from soybean stalk in continuous feed reactor. INTERNATIONAL JOURNAL OF AGRICULTURAL ENGINEERING 2015;8(1):26-30.

44. Ahmed Al-Jumaili, Surjith Alancherry, Kateryna Bazaka, Mohan V Jacob. Review on the Antimicrobial Properties of Carbon Nanostructures. Materials (Basel, Switzerland) 2017;10(9):1066.

45. Husain S, Koros WJ. Mixed matrix hollow fiber membranes made with modified HSSZ-13 zeolite in polyetherimide polymer matrix for gas separation. Journal of Membrane Science 2007;288(1):195-207.

46. Hosseini SM, Amini SH, Khodabakhshi AR, Bagheripour E, Van der Bruggen B. Activated carbon nanoparticles entrapped mixed matrix polyethersulfone based nanofiltration

membrane for sulfate and copper removal from water. Journal of the Taiwan Institute of Chemical Engineers 2018;82:169-178.

47. Abu-Bakar AS, Moinuddin K. Effects of variation in heating rate, sample mass and nitrogen flow on chemical kinetics for pyrolysis. : Australasian Fluid Mechanics Society, Dec 2012.

48. Gabhi RS, Kirk DW, Jia CQ. Preliminary investigation of electrical conductivity of monolithic biochar. Carbon 2017;116:435-442.

49. Zhang L, Li Y, Zhou J. Anisotropic Dielectric Properties of Carbon Fiber Reinforced Polymer Composites during Microwave Curing. Applied Composite Materials 2018;25(6):1339-1356.

50. Mohammad Hassan, Ragab Abou-Zeid, Enas Hassan, Linn Berglund, Yvonne Aitomäki, Kristiina Oksman. Membranes Based on Cellulose Nanofibers and Activated Carbon for Removal of Escherichia coli Bacteria from Water. Polymers 2017;9(8):335.

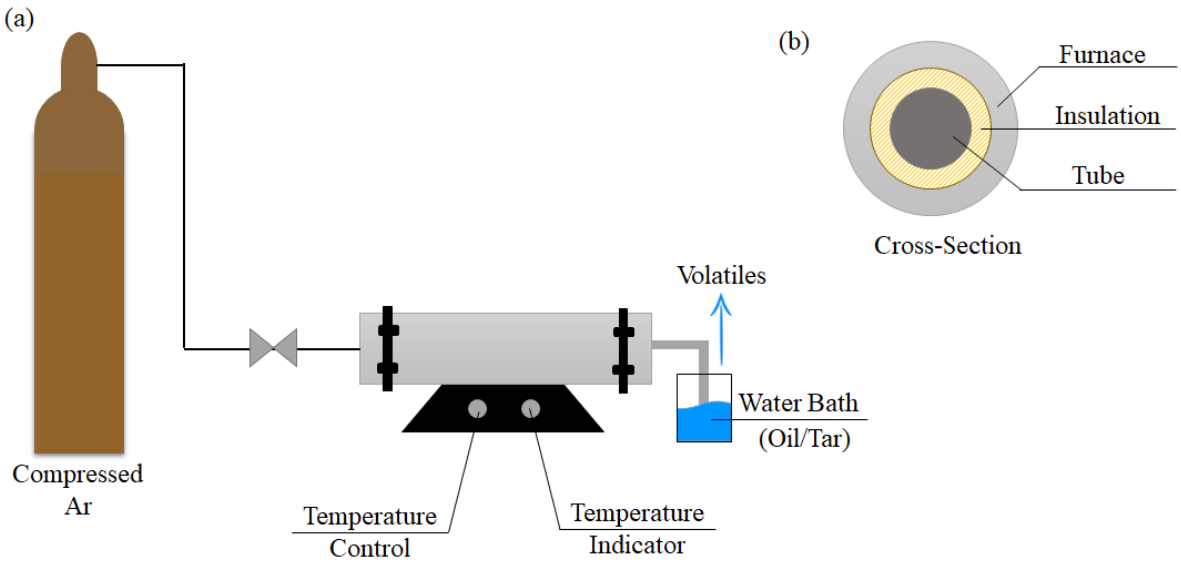


Figure 1: (a) Pyrolysis reactor set-up schematic and (b) cross-sectional view of furnace.

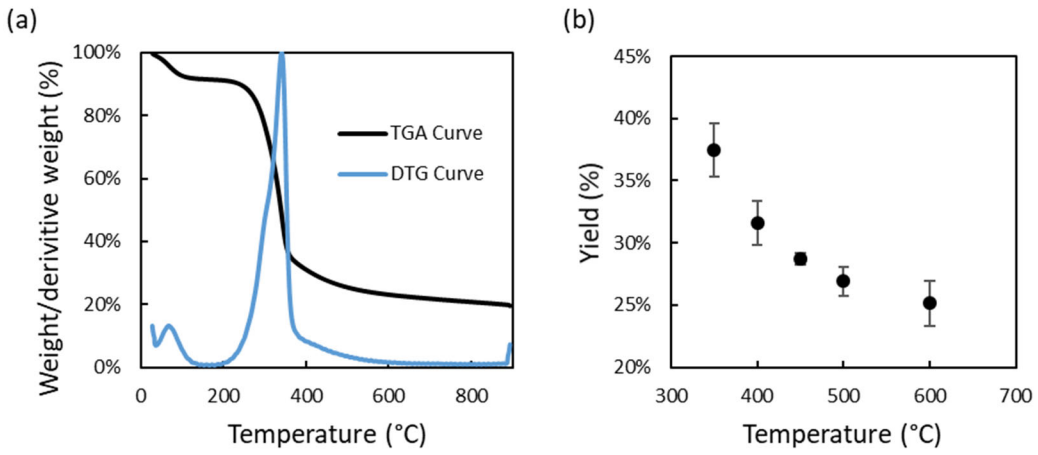


Figure 2: (a) TGA and DTG curves of the raw SSH and (b) biochar yield as a function of temperature after pyrolysis.

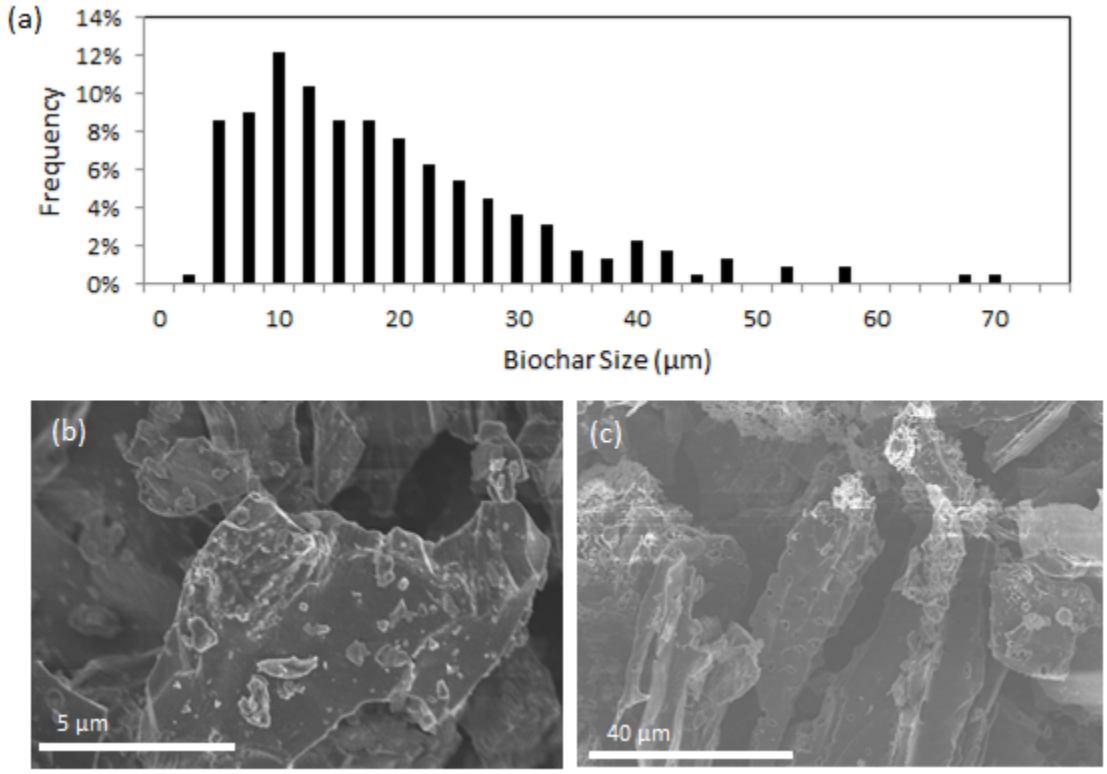


Figure 3: (a) size distribution of biochar ignoring aggregates less than 2.5 microns. (b) SEM image depicting aggregate formation, (c) irregular shaped particles, and pore formation.

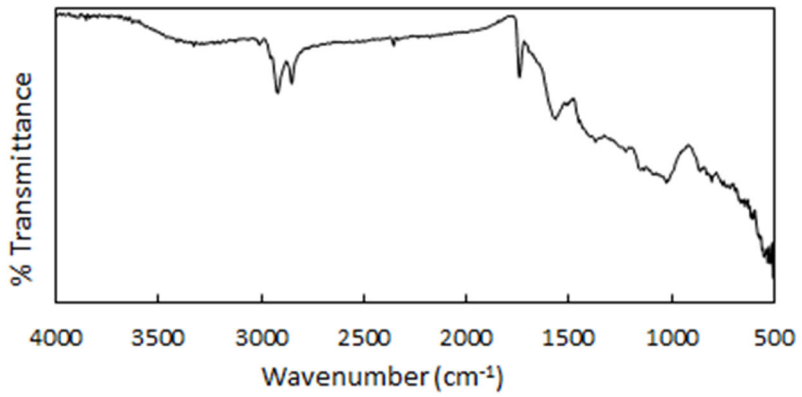


Figure 4: FTIR spectra of biochar created from pyrolysis of SSH at 500°C.

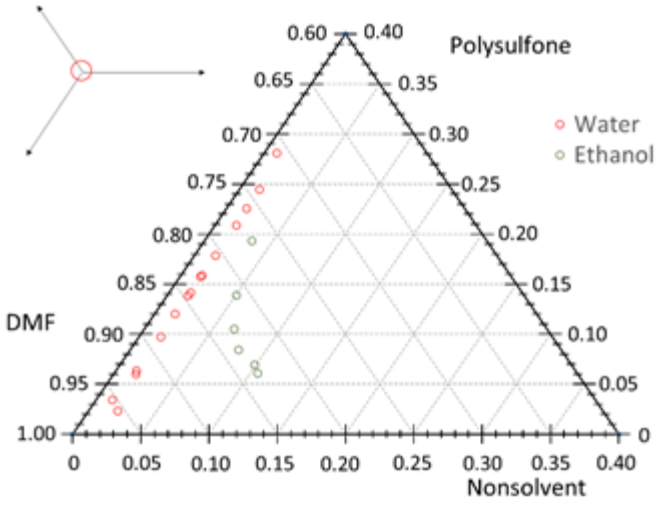


Figure 5: Ternary phase diagram with experimentally determined binodal lines using pure water and pure ethanol as nonsolvent in DMF/PSF/Nonsolvent system. All fractions are by weight and the key in the top left demonstrates the relationship between each point and its corresponding grid lines.

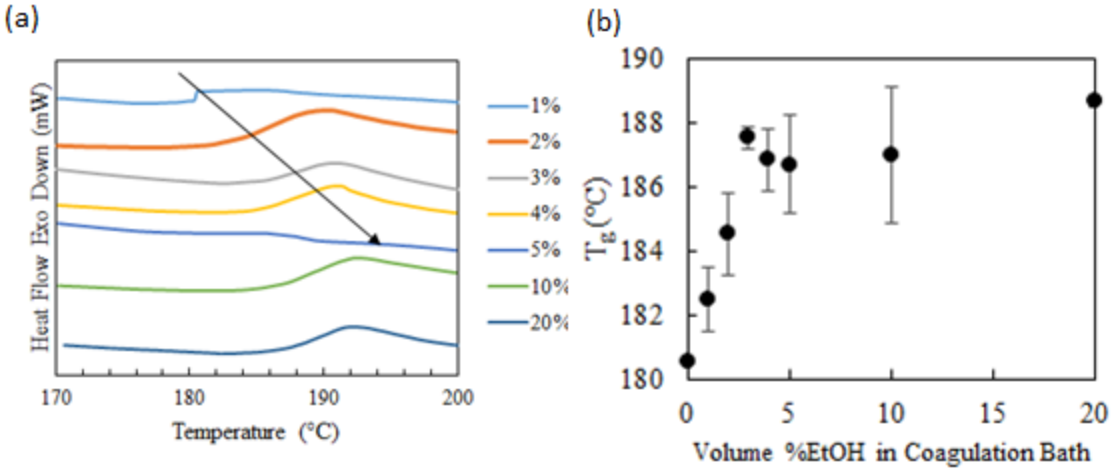


Figure 6: (a) DSC thermograms and (b) extracted $T_g$ data as a function of vol.% ethanol in coagulation bath at 95% confidence.

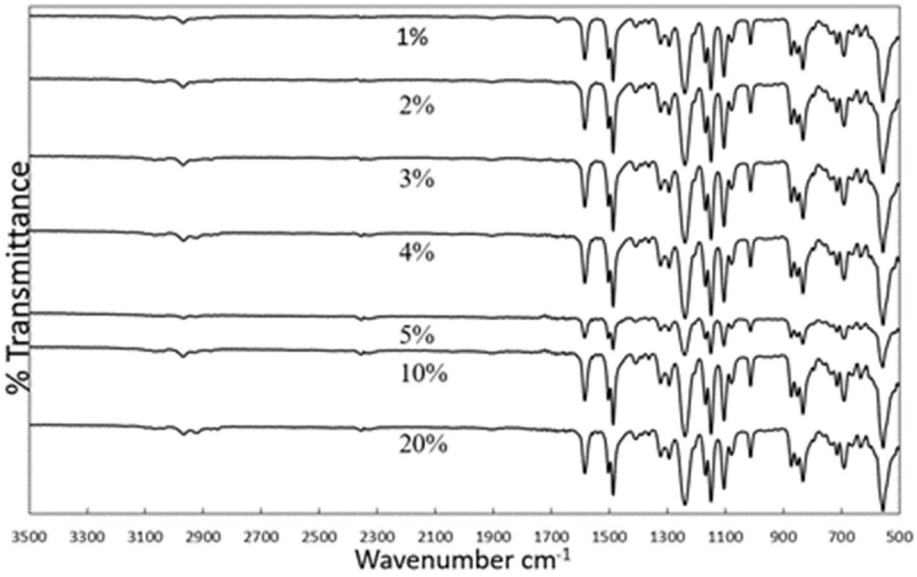


Figure 7: FTIR spectra of MMMs made with 1-20 vol.% ethanol in the coagulation bath.

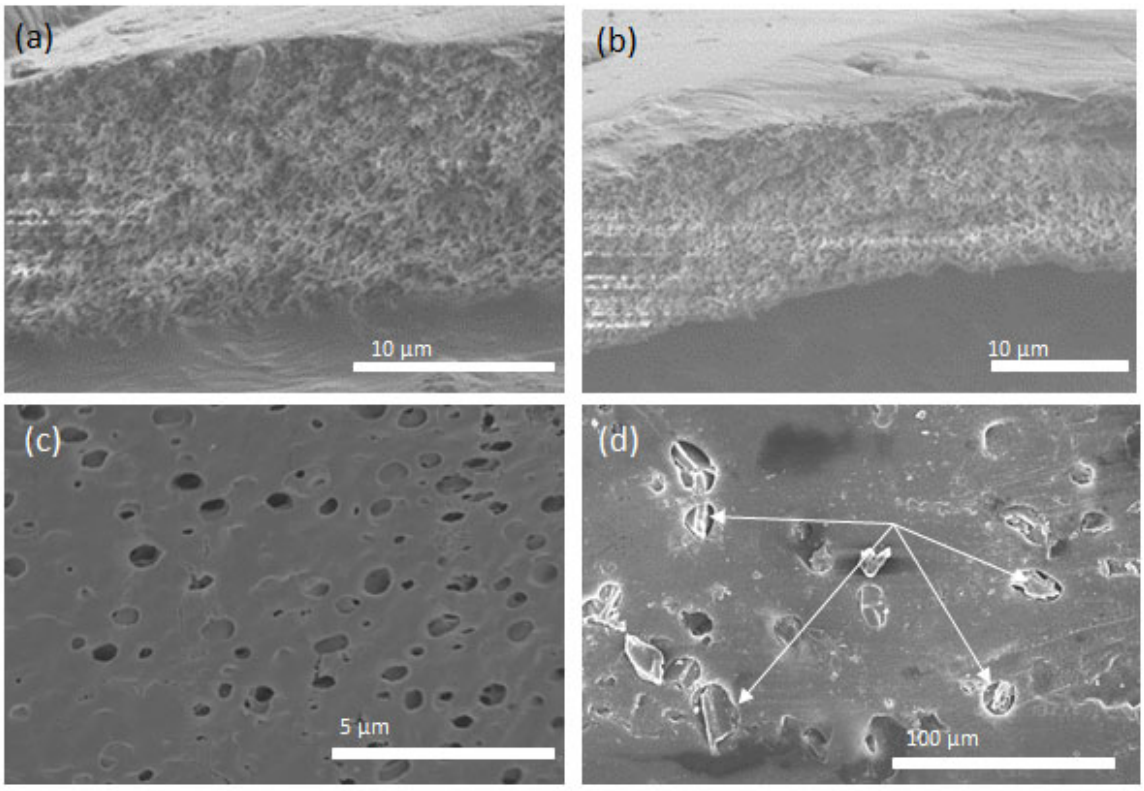


Figure 8: Cross sectional view of films made with (a) 0% and (b) 4% ethanol. Surface view showing (c) pore formation with 10% loading and (d) pore blockage at 40% biochar loading.

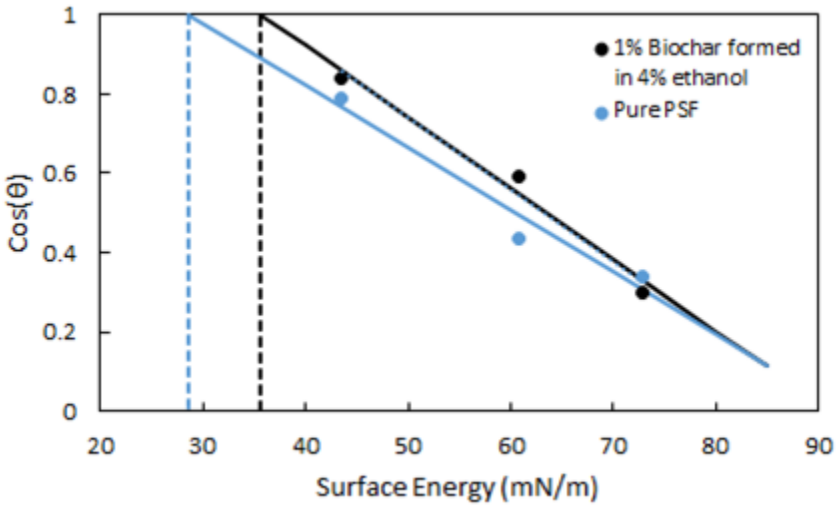


Figure 9: Zisman plot for each film showing extrapolated values for the 1% biochar ($\gamma_c$=35.7 mN/m, $R^2$ = 0.9761) and pure PSF ($\gamma_c$=28.6 mN/m, $R^2$ = 0.9519).

Table 1: Ultimate and proximate analysis of raw SSH and biochar produced at 500°C, and physical properties of biochar. All percentages are by weight.

| Property | Raw SSH | Biochar |
|---|---|---|
| C (%) | 48.24 | 65.93 |
| H (%) | 5.84 | 3.54 |
| N (%) | 0.30 | 2.00 |
| O*(%) | 41.16 | 17.25 |
| Moisture (%) | 3.45 | 2.60 |
| Volatiles (%) | 81.90 | 36.06 |
| Ash (%) | 4.46 | 11.28 |
| Fixed Carbon* (%) | 10.19 | 50.06 |
| Iodine Number (mg/g) | - | 203 |
| Pore Volume (mL/g) | - | 0.595 |

*denotes calculation by difference.

Table 2: Summary of FTIR spectra of biochar

| **Peak Location ($cm^{-1}$)** | **Functional Group** | **Molecular Motion** |
|---|---|---|
| 3300 | Alcohols | -OH stretch |
| 2900-2850 | Alkane | $CH_3$ stretch |
| 2350 | Alkyne or Nitrile | C≡C stretch, C≡N stretch |
| 1740 | Aldehyde or Ester | C=O stretch |
| 1650 | Amide or Carboxylate | $CO_2$ stretch |
| 1370 | Aldehyde | C-H bend |
| 1220 | Ester | C-C-O stretch |
| 1130 | Ester | O-C-C stretch |
| <1000 | Aromatic | C=C, $NH_2$ wag, C-C stretch, C-O bend, N-O bend, N-H bend, O-H bend, C-H stretch |

Table 3: Measured contact angle on each surface, and liquid surface energy values used for analysis. The contact angles reported are the average of at least two measurements at a 95% confidence level.

| Liquid | $\gamma_l$ (mN/m) | Contact angle (°) | |
|---|---|---|---|
| | | Pure PSF | 1% Loaded Biochar in 4% Ethanol |
| Distilled Water | 72.80 [41] | 70.01 ± 2.0 | 72.56 ± 2.0 |
| 15% PEG-200 | 60.79 [41] | 64.14 ± 2.1 | 53.59 ± 0.5 |
| PEG-200 | 43.50 [42] | 37.67 ± 1.5 | 33.08 ± 0.5 |